

Online unmixing of multitemporal hyperspectral images accounting for spectral variability

Pierre-Antoine Thouvenin, *Student Member, IEEE*, Nicolas Dobigeon, *Senior Member, IEEE* and Jean-Yves Tourneret, *Senior Member, IEEE*

Abstract

Hyperspectral unmixing is aimed at identifying the reference spectral signatures composing an hyperspectral image – referred to as *endmembers* – and their relative abundance fractions in each pixel. In practice, the identified signatures may vary spectrally from an image to another due to varying acquisition conditions inducing possibly significant estimation errors. Against this background, hyperspectral unmixing of several images acquired over the same area is of considerable interest. Indeed, such an analysis enables the endmembers of the scene to be tracked and the corresponding endmember variability to be characterized. Sequential endmember estimation from a set of hyperspectral images is expected to provide improved performance when compared to methods analyzing the images independently. However, the significant size of hyperspectral data precludes the use of batch procedures to jointly estimate the mixture parameters of a sequence of hyperspectral images. Provided that each elementary component is present in at least one image of the sequence, we propose to perform an online hyperspectral unmixing accounting for temporal endmember variability. The online hyperspectral unmixing is formulated as a two-stage stochastic program, which can be solved using a classical stochastic approximation. The performance of the proposed method is evaluated on synthetic and real data. A comparison with independent unmixings of each image by state-of-the-art methods finally illustrates the interest of the proposed strategy.

Index Terms

Hyperspectral imagery, perturbed linear unmixing (PLMM), endmember temporal variability, two-stage stochastic program, stochastic approximation (SA).

This work is supported by the Direction Générale de l'Armement, French Ministry of Defence.

The authors are with the University of Toulouse, IRIT/INP-ENSEEIHT, 2 rue Camichel, BP 7122, 31071 Toulouse cedex 7, France. (e-mail: {pierreantoine.thouvenin, Nicolas.Dobigeon, Jean-Yves.Tourneret}@enseeiht.fr)

I. INTRODUCTION

Hyperspectral imagery has known an increasing interest over the past decades due to the significant spectral information it conveys. Acquired in hundreds of contiguous spectral bands from 300 nm to 2600 nm, hyperspectral (HS) images facilitate the identification of the elements composing the imaged scene. However, the high spectral resolution of these images is mitigated by their lower spatial resolution, which results in pixel spectra composed of mixtures of reference signatures. Spectral unmixing consists of determining the reference spectral signatures composing the data – referred to as *endmembers* – and their abundance fractions in each pixel according to a predefined mixture model accounting for several environmental factors (declivity, multiple reflections, ...). Provided microscopic interactions between the materials of the imaged scene are negligible and the relief of the scene is flat, a linear mixing model (LMM) is traditionally used to describe the data [1]. However, varying acquisition conditions such as illumination or natural evolution of the scene may significantly alter the shape and the amplitude of the spectral signatures acquired, thus affecting the extracted endmembers from an image to another. In this context, HS unmixing of several images acquired over the same area at different time instants can be of considerable interest. Indeed, such an analysis enables the endmembers of the scene and endmember variability to be assessed, thus improving endmember estimation when compared to independent image analyses performed with any state-of-the-art unmixing method.

So far, spatial variability within a given image has been considered in various models either derived from a statistical or a deterministic point of view [2]. The first class of methods assumes that the endmember spectra are realizations of multivariate distributions [3]–[5]. The second class of methods represents endmember signatures as members of spectral libraries associated with each material (bundles) [6]. Another recently proposed approach consists in estimating the parameters of an explicit variability model [7]. To the best of our knowledge, spatio-temporal variability has been analyzed for the first time in the Bayesian framework proposed in [8]. Nevertheless, HS unmixing using a significant number of images or several large images precludes the use of batch estimation procedures due to limited memory and computational resources. In this work, we focus on the design of an online HS unmixing method accounting for temporal variability.

Since the identified endmembers can be considered as time-varying instances of reference end-members, we use the perturbed linear mixing model (PLMM) proposed in [7] to account for spectral variability. However, inspired by the works presented in [9], [10], we formulate the unmixing problem as a two-stage stochastic program that allows the model parameters to be estimated online, contrary to the algorithm proposed in [7]. To the best of our knowledge, it is the first time HS unmixing accounting for temporal variability has been formulated as a two-stage stochastic program and solved

TABLE I
NOTATIONS.

N	number of pixels
L	number of spectral bands
K	number of endmembers
T	number of images
$\mathbf{y}_{nt} \in \mathbb{R}^L$	n th pixel of the t th image
$\mathbf{Y}_t \in \mathbb{R}^{L \times N}$	lexicographically ordered pixels of the t th image
$\mathbf{M} \in \mathbb{R}^{L \times K}$	endmember matrix
$\mathbf{dM}_t \in \mathbb{R}^{L \times K}$	t th variability matrix
$\mathbf{A}_t \in \mathbb{R}^{K \times N}$	t th abundance matrix
$\mathbf{a}_{nt} \in \mathbb{R}^K$	n th column of the matrix \mathbf{A}_t
\succeq	term-wise inequality
\mathcal{Y}	$[0, 1]^{L \times N}$
\mathcal{M}	$[0, 1]^{L \times K}$
\mathcal{S}_K	unit simplex of \mathbb{R}^K
\mathcal{A}_K	$\{\mathbf{A} \in \mathbb{R}^{K \times N} \mid \mathbf{a}_n \in \mathcal{S}_K, \forall n \in \llbracket 1, N \rrbracket\}$
$\mathcal{B}_F(\mathbf{0}, \sigma)$	$\{\mathbf{X} \in \mathbb{R}^{L \times K} \mid \ \mathbf{X}\ _F \leq \sigma\}$
$\mathcal{B}_F(\mathbf{Z}, \kappa)$	$\{\mathbf{X} \in \mathbb{R}^{L \times K} \mid \ \mathbf{X} - \mathbf{Z}\ _F \leq \kappa\}$
\mathcal{D}	$\mathcal{B}_F(\mathbf{0}, \sigma) \cap \{\mathbf{dM} \mid \ \mathbb{E}_\omega[\mathbf{dM}(\omega)]\ _F \leq \kappa\}$
\mathcal{D}_t	$\mathcal{B}_F(\mathbf{0}, \sigma) \cap \{\mathbf{dM}_t \mid \ \sum_{i=1}^t \mathbf{dM}_i\ _F \leq \kappa\}$
$\mathcal{Q}_t(\mathbf{Y}, \mathbf{M})_t$	$\{(\mathbf{A}, \mathbf{dM}) \in \mathcal{D}_t \mid \nabla_{(\mathbf{A}, \mathbf{dM})} f(\mathbf{Y}, \mathbf{M}, \mathbf{A}, \mathbf{dM}) = \mathbf{0}\}$
$\mathcal{P}_{\mathcal{S}}$	projector on the set \mathcal{S}
\mathcal{P}_+	projector on $\{\mathbf{X} \in \mathbb{R}^{L \times K} \mid \mathbf{X} \succeq \mathbf{0}_{L, K}\}$
$\langle \cdot, \cdot \rangle$	canonical scalar product on euclidean matrix spaces.

using an online algorithm.

The paper is organized as follows. The PLMM accounting for temporal variability is introduced in Section II. Section III describes an online algorithm to solve the resulting optimization problem. Experimental results obtained on synthetic and real data are reported in Sections IV and V respectively. The results obtained with the proposed algorithm are systematically compared to those of the vertex component analysis / fully constrained least squares (VCA [11] / SUNSAL [12]) and SISAL [13] / SUNSAL [12] independently applied to each image of the sequence. Section VI finally concludes this work.

II. PROBLEM STATEMENT

A. Perturbed linear mixing model (PLMM)

Let consider T HS images acquired at different time instants over the same scene, assuming that at most K endmembers are present in the resulting time series and that the images share these K common endmembers. Note that each endmember does not need to be present in each image, but at least in one image of the time series. Given an *a priori* known number of endmembers K , the PLMM consists in representing each pixel \mathbf{y}_{nt} by a linear combination of the K endmembers – denoted as \mathbf{m}_k – affected by a perturbation vector \mathbf{dm}_{kt} accounting for temporal endmember variability. The resulting PLMM can be written

$$\mathbf{y}_{nt} = \sum_{k=1}^K a_{knt} (\mathbf{m}_k + \mathbf{dm}_{kt}) + \mathbf{b}_{nt} \quad (1)$$

for $n = 1, \dots, N$ and $t = 1, \dots, T$, where \mathbf{y}_{nt} denotes the n th image pixel at time t , \mathbf{m}_k is the k th endmember, a_{knt} is the proportion of the k th endmember in the n th pixel at time t , and \mathbf{dm}_{kt} denotes the perturbation of the k th endmember at time t . Finally, \mathbf{b}_{nt} models the noise resulting from the data acquisition and the modeling errors. In matrix form, the PLMM (1) can be written as

$$\mathbf{Y}_t = (\mathbf{M} + \mathbf{dM}_t) \mathbf{A}_t + \mathbf{B}_t \quad (2)$$

where $\mathbf{Y}_t = [\mathbf{y}_{1t}, \dots, \mathbf{y}_{Nt}]$ is an $L \times N$ matrix containing the pixels of image $\#t$, \mathbf{M} denotes an $L \times K$ matrix containing the endmembers, \mathbf{A}_t is a $K \times N$ matrix composed of the abundance vectors \mathbf{a}_{nt} , \mathbf{dM}_t is an $L \times K$ matrix whose columns are the perturbation vectors associated with the image $\#t$, and \mathbf{B}_t is an $L \times N$ matrix accounting for the noise at time instant t . The non-negativity and sum-to-one constraints usually considered to reflect physical considerations are

$$\begin{aligned} \mathbf{A}_t &\succeq \mathbf{0}_{K,N}, \quad \mathbf{A}_t^T \mathbf{1}_K = \mathbf{1}_N, \quad \forall t = 1, \dots, T \\ \mathbf{M} &\succeq \mathbf{0}_{L,K} \end{aligned} \quad (3)$$

where \succeq denotes a term-wise inequality. We also consider the following assumptions on the inherent variability of the observed scenes

$$\|\mathbf{dM}_t\|_F^2 \leq \sigma^2, \quad \text{for } t = 1, \dots, T \quad (4)$$

$$\left\| \sum_{t=1}^T \mathbf{dM}_t \right\|_F^2 \leq \kappa^2 \quad (5)$$

where σ and κ are fixed positive constants, and $\|\cdot\|_F$ denotes the Frobenius norm. These two constraints can be interpreted in terms of the feasible domain of \mathbf{M} and \mathbf{dM}_t . Indeed, introducing the perturbed endmembers $\mathbf{M}_t \triangleq \mathbf{M} + \mathbf{dM}_t$, the constraint (4) can be reformulated as

$$\|\mathbf{dM}_t\|_F^2 = \|\mathbf{M} - \mathbf{M}_t\|_F^2 \leq \sigma^2 \Leftrightarrow \mathbf{M} \in \bigcap_{t=1}^T \mathcal{B}_F(\mathbf{M}_t, \sigma)$$

where $\mathcal{B}_F(\mathbf{M}_t, \sigma)$ is the ball of center \mathbf{M}_t and of radius σ . On the other hand, (5) constrains the perturbed endmembers to be distributed around the true endmembers, i.e., the endmember signatures \mathbf{M} should reflect the mean behavior of the perturbed endmembers \mathbf{M}_t over the sequence. This implicitly results in an endmember estimation improvement as T increases, since the endmembers belong to a set whose size decreases with the number of images analyzed.

Remark 1. In practice, HS unmixing is performed on reflectance data, hence $\mathbf{Y}_t \in [0, 1]^{L \times N}$. The abundance sum-to-one and non-negativity constraints further imply $\mathbf{M} \in [0, 1]^{L \times K}$. In fact, the compactness of both the data support and the space associated with the constraints relative to the endmembers – denoted by \mathcal{Y} and \mathcal{M} respectively – is crucial for the convergence result given in Paragraph III-C.

B. Problem formulation

In order to design an online estimation algorithm, the model (1) combined with the constraints (3) can be used to formulate a two-stage stochastic program consisting in estimating the endmembers present in the image sequence. Since only the endmembers are supposed to be commonly shared by the different images, we propose to minimize a marginal cost function obtained by marginalizing an instantaneous cost function over the abundances and the variability terms, so that the resulting cost only depends on the endmembers. Assuming the expectations are well-defined, we consider the following optimization problem

$$\min_{\mathbf{M} \in \mathcal{M}} g(\mathbf{M}) = \mathbb{E}_{\mathbf{Y}, \mathbf{A}, \mathbf{dM}} \left[f(\mathbf{Y}, \mathbf{M}, \mathbf{A}, \mathbf{dM}) \right] \quad (6)$$

where $\mathcal{M} = [0, 1]^{L \times K}$. We propose to define the function f of (6) as

$$\begin{aligned} f(\mathbf{Y}, \mathbf{M}, \mathbf{A}, \mathbf{dM}) = & \frac{1}{2} \|\mathbf{Y} - (\mathbf{M} + \mathbf{dM})\mathbf{A}\|_F^2 \\ & + \alpha\Phi(\mathbf{A}) + \beta\Psi(\mathbf{M}) + \gamma\Upsilon(\mathbf{dM}) \end{aligned} \quad (7)$$

where Φ , Ψ and Υ denote appropriate penalization terms on the abundances, the endmembers and the variability and

$$\mathbf{A} \in \mathcal{A}_K = \left\{ \mathbf{A} \in \mathbb{R}^{K \times N} \mid \mathbf{a}_n \in \mathcal{S}_K, \text{ for } n = 1, \dots, N \right\} \quad (8)$$

$$\mathbf{dM} \in \mathcal{D} = \mathcal{B}_F(\mathbf{0}, \sigma) \cap \left\{ \mathbf{dM} \mid \|\mathbb{E}[\mathbf{dM}]\|_F \leq \kappa \right\}. \quad (9)$$

The parameters α, β and γ ensure a trade-off between the data fitting term and the penalties. In practice, g is approximated at time t by an upper bound \hat{g}_t given by a stochastic approximation [10]

$$\begin{aligned}
\hat{g}_t(\mathbf{M}) &= \frac{1}{2t} \sum_{i=1}^t \|\mathbf{Y}_i - (\mathbf{M} + \mathbf{dM}_i)\mathbf{A}_i\|_F^2 + \beta\Psi(\mathbf{M}) \\
&= \frac{1}{t} \sum_{i=1}^t \left(\frac{1}{2} \|\mathbf{MA}_i\|_F^2 - \langle \mathbf{Y}_i - \mathbf{dM}_i\mathbf{A}_i, \mathbf{MA}_i \rangle \right) \\
&\quad + \beta\Psi(\mathbf{M}) + c \\
&= \frac{1}{t} \left[\frac{1}{2} \text{Tr}(\mathbf{M}^T \mathbf{MC}_t) + \text{Tr}(\mathbf{M}^T \mathbf{D}_t) \right] + \beta\Psi(\mathbf{M}) + c
\end{aligned} \tag{10}$$

where c is a constant independent from \mathbf{M} and

$$\mathbf{C}_t = \sum_{i=1}^t \mathbf{A}_i \mathbf{A}_i^T, \quad \mathbf{D}_t = \sum_{i=1}^t (\mathbf{dM}_i \mathbf{A}_i - \mathbf{Y}_i) \mathbf{A}_i^T. \tag{11}$$

Besides, \mathcal{D} is approximated by

$$\mathcal{D}_t = \mathcal{B}_F(\mathbf{0}, \sigma) \cap \{\mathbf{dM}_t \mid \|\mathbf{dM}_t + \mathbf{E}_{t-1}\|_F \leq \kappa\} \tag{12}$$

with

$$\mathbf{E}_t = \sum_{i=1}^t \mathbf{dM}_i. \tag{13}$$

Examples of penalizations that will be considered in this study are detailed in the following paragraphs.

1) *Abundance penalization*: In this work, the abundance penalization Φ has been chosen to promote temporally smooth abundances – in the ℓ_2 -norm sense – between two consecutive images, leading to

$$\Phi(\mathbf{A}_t) = \frac{1}{2} \|\mathbf{A}_t - \mathbf{A}_{t-1}\|_F^2. \tag{14}$$

As long as Φ satisfies the regularity condition given in Paragraph III-C, any other type of prior knowledge relative to the abundances can be incorporated into the proposed method.

2) *Endmember penalization*: Classical endmember penalizations found in the literature consist in constraining the size of the $(K - 1)$ -simplex whose vertices are the endmembers. In this paper, we consider the mutual distance between each endmember introduced in [14], [15], defined as

$$\Psi(\mathbf{M}) = \frac{1}{2} \sum_{i=1}^K \left(\sum_{\substack{j=1 \\ j \neq i}}^K \|\mathbf{m}_i - \mathbf{m}_j\|_2^2 \right) = \frac{1}{2} \sum_{k=1}^K \|\mathbf{MG}_k\|_F^2 \tag{15}$$

where

$$\mathbf{G}_k = -\mathbf{I}_K + \mathbf{e}_k \mathbf{1}_K^T \tag{16}$$

and \mathbf{e}_k denotes the k th canonical basis vector of \mathbb{R}^K .

Algorithm 1: Online unmixing algorithm.

Data: $\mathbf{M}_0, \mathbf{A}_0, \mathbf{dM}_0, \alpha > 0, \beta > 0, \gamma > 0, \xi \in]0, 1]$

begin

$\mathbf{C}_0 \leftarrow \mathbf{0}_{K,K};$

$\mathbf{D}_0 \leftarrow \mathbf{0}_{L,K};$

$\mathbf{E}_0 \leftarrow \mathbf{0}_{L,K};$

for $t = 1$ **to** T **do**

 a

 Random selection of an image \mathbf{Y}_t ;

 // Abundance and variability estimation by PALM [16], cf. §III-B1

 b

$(\mathbf{A}_t, \mathbf{dM}_t) \in \arg \min_{(\mathbf{A}, \mathbf{dM}) \in \mathcal{A}_K \times \mathcal{D}_t} f(\mathbf{Y}_t, \mathbf{M}_t, \mathbf{A}, \mathbf{dM});$

$\mathbf{C}_t \leftarrow \xi \mathbf{C}_{t-1} + \mathbf{A}_t \mathbf{A}_t^T$;

$\mathbf{D}_t \leftarrow \xi \mathbf{D}_{t-1} + (\mathbf{dM}_t \mathbf{A}_t - \mathbf{Y}_t) \mathbf{A}_t^T$;

$\mathbf{E}_t \leftarrow \xi \mathbf{E}_{t-1} + \mathbf{dM}_t$;

 // Endmember update [10, Alg. 2], cf. §III-B2

 c

$\mathbf{M}^{(t)} \leftarrow \arg \min_{\mathbf{M} \in \mathcal{M}} \hat{g}_t(\mathbf{M})$;

Result: $\mathbf{M}^{(T)}, (\mathbf{A}_t)_{t=1, \dots, T}, (\mathbf{dM}_t)_{t=1, \dots, T}$

3) *Variability penalization:* Assuming that the spectral variation between two consecutive images is *a priori* temporally smooth, we consider the following ℓ_2 -norm penalization

$$\Upsilon(\mathbf{dM}_t) = \frac{1}{2} \|\mathbf{dM}_t - \mathbf{dM}_{t-1}\|_F^2. \quad (17)$$

Similarly, any other type of prior knowledge relative to the variability can be considered as long as Υ satisfies the regularity condition given in Paragraph III-C.

III. A TWO-STAGE STOCHASTIC PROGRAM

A. Two-stage stochastic program: general principle

The following lines briefly recall the main ideas presented in the introduction of [9]. A two-stage stochastic program is generally expressed as

$$\min_{\mathbf{M}} \mathbb{E}_{\mathbf{Y}, \mathbf{Z}} [f(\mathbf{Y}, \mathbf{M}, \mathbf{Z})] \text{ s.t. } \mathbf{M} \in \mathcal{M}, \text{ with } \mathbf{Z} \in \mathcal{Z}. \quad (18)$$

At the first stage, \mathbf{M} must be chosen before any new data \mathbf{Y} is available. At the second-stage, when \mathbf{M} has been fixed and a new data is acquired, the second-stage variable \mathbf{Z} is computed as the solution (if it is unique and well defined) to the optimization problem

$$\min_{\mathbf{Z} \in \mathcal{Z}} f(\mathbf{Y}, \mathbf{M}, \mathbf{Z}). \quad (19)$$

Given an independent and identically distributed (i.i.d) T -sample $(\mathbf{Y}_1, \dots, \mathbf{Y}_T)$, problem (18) can be approximated by the sample average approximation (SAA)

$$\min_{\mathbf{M}, \mathbf{Z}_1, \dots, \mathbf{Z}_T} \frac{1}{T} \sum_{t=1}^T f(\mathbf{Y}_t, \mathbf{M}, \mathbf{Z}_t), \text{ s.t. } \mathbf{M} \in \mathcal{M}, \mathbf{Z}_t \in \mathcal{Z}. \quad (20)$$

Moreover, when the second-stage (19) admits a unique solution, (20) can be rewritten as

$$\min_{\mathbf{M} \in \mathcal{M}} \frac{1}{T} \sum_{t=1}^T h(\mathbf{Y}_t, \mathbf{M}) \quad (21)$$

$$h(\mathbf{Y}_t, \mathbf{M}) = \min_{\mathbf{Z}_t \in \mathcal{Z}} f(\mathbf{Y}_t, \mathbf{M}, \mathbf{Z}_t) \quad (22)$$

which is the SAA corresponding to

$$\min_{\mathbf{M} \in \mathcal{M}} \mathbb{E}_{\mathbf{Y}} [h(\mathbf{Y}, \mathbf{M})] \quad (23)$$

$$h(\mathbf{Y}, \mathbf{M}) = \min_{\mathbf{Z} \in \mathcal{Z}} f(\mathbf{Y}, \mathbf{M}, \mathbf{Z}) \quad (24)$$

where the two stages explicitly appear. However, f defined in (7) is not (strictly) convex with respect to $\mathbf{Z} = (\mathbf{A}, \mathbf{dM})$. Thus, problem (19) does not admit a unique global minimum, and existing algorithms will at most provide a critical point of f . In this specific case, a new convergence framework based on a generalized equation has been developed in [9].

Such a framework enables a convergence result in terms of a critical point $\{\mathbf{M}, \mathbf{Z}_1, \dots, \mathbf{Z}_T\}$ of (20) to be obtained. However, the significant size of the SAA problem (20) in our case is generally too expensive from a computational point of view. To alleviate this problem, we propose to slightly adapt the work developed in [10] to develop an online estimation algorithm described by Algo.1. This algorithm has the same convergence property as [10] thereby assuming the non-convex function $f(\mathbf{Y}, \mathbf{M}, \cdot, \cdot)$ exclusively admits locally unique critical points. Further details are given in Paragraph III-C.

B. Parameter estimation

Whenever an image \mathbf{Y}_t has been received, the abundances and variability are estimated by a proximal alternating linearized minimization (PALM) [16], which is guaranteed to converge to a critical point of $f(\mathbf{Y}_t, \mathbf{M}_t, \cdot, \cdot)$. The endmembers are then updated by proximal gradient descent steps, similarly to [10].

1) Abundance and variability estimation: A direct application of [16] under the constraints (3) leads to the following abundance update rule

$$\mathbf{A}_t^{(k+1)} = \mathcal{P}_{\mathcal{A}_K} \left(\mathbf{A}_t^{(k)} - \frac{1}{\lambda_t^{(k)}} \nabla_{\mathbf{A}} f(\mathbf{Y}_t, \mathbf{M}_t, \mathbf{A}_t^{(k)}, \mathbf{dM}_t^{(k)}) \right) \quad (25)$$

$$\lambda_t^{(k)} = \gamma_1 L_{1t}^{(k)}, \quad \gamma_1 > 1 \quad (26)$$

Algorithm 2: Abundance and variability estimation using PALM.

Data: $\mathbf{Y}, \mathbf{M}, \mathbf{A}^{(0)}, \mathbf{dM}^{(0)}, \mathbf{E}, \gamma_1 > 1, \gamma_3 > 1$

begin

$k \leftarrow 0;$

while *stopping criterion not satisfied* **do**

// Abundance update

$$\mathbf{A}^{(k+1)} \leftarrow \text{Update} \left(\mathbf{A}^{(k)} \right) ;$$

```
// Variability update
```

$$\mathbf{dM}^{(k+1)} \leftarrow$$

$$\mathbf{A} \leftarrow \mathbf{A}^{(k)} \quad \mathbf{dM} \leftarrow \mathbf{dM}^{(k)} \quad .$$

Result: (A, dM)

where $L_{1t}^{(k)}$ is the Lipschitz constant of $\nabla_{\mathbf{M}} f(\mathbf{Y}_t, \mathbf{M}_t, \cdot, d\mathbf{M}_t^{(k)})$ and

$$\nabla_{\mathbf{A}} f(\mathbf{Y}_t, \mathbf{M}_t, \mathbf{A}_t, d\mathbf{M}_t) = (\mathbf{M}_t + d\mathbf{M}_t)^T [(\mathbf{M}_t + d\mathbf{M}_t)\mathbf{A}_t - \mathbf{Y}_t] + \alpha(\mathbf{A}_t - \mathbf{A}_{t-1}) \quad (27)$$

$$L_{1t}^{(k)} = \left\| (\mathbf{M}_t + \mathbf{dM}_t^{(k)})^\top (\mathbf{M}_t + \mathbf{dM}_t^{(k)}) + \alpha \mathbf{I}_K \right\|^2. \quad (28)$$

Note that the projection $\mathcal{P}_{\mathcal{A}_K}$ can be exactly computed using the algorithms proposed in [17], [18].

Similarly, the update rule for the variability terms is

$$\begin{aligned} d\mathbf{M}_t^{(k+1)} = \\ \mathcal{P}_{\mathcal{D}_t} \left(d\mathbf{M}_t^{(k)} - \frac{1}{(k)} \nabla_{d\mathbf{M}} f(\mathbf{Y}_t, \mathbf{M}_t, \mathbf{A}_t^{(k+1)}, d\mathbf{M}_t^{(k)}) \right) \end{aligned} \quad (29)$$

$$u^{(k)} = \gamma_2 L^{(k)} \quad \gamma_2 > 1 \quad (30)$$

where $L_{\mathcal{S}}^{(k)}$ is the Lipschitz constant of $\nabla_{\mathbf{A}, \mathbf{M}} f(\mathbf{Y}, \mathbf{M}, \mathbf{A}^{(k+1)}, \cdot)$ and

$$\nabla_{\mathbf{dM}} f(\mathbf{Y}_t, \mathbf{M}_t, \mathbf{A}_t, \mathbf{dM}_t) = \quad (21)$$

$$[(\mathbf{M}_t + d\mathbf{M}_t) \mathbf{A}_t - \mathbf{Y}_t] \mathbf{A}_t^T + \gamma(d\mathbf{M}_t - d\mathbf{M}_{t-1})$$

$$L_{3t}^{(k)} = \left\| \mathbf{A}_t^{(k+1)} \mathbf{A}_t^{(k+1)\top} + \gamma \mathbf{I}_K \right\|^2. \quad (32)$$

Note that the projection $\mathcal{P}_{\mathcal{D}_t}$ can be efficiently computed (see [19]). The resulting algorithm is summarized in Algo. 2.

Algorithm 3: Endmember estimation.

Data: $\mathbf{M}^{(0)}, \mathbf{C}, \mathbf{D}, \gamma_2 > 1$

begin

$k \leftarrow 0;$

while stopping criterion not satisfied **do**

// Endmember update

$\mathbf{M}^{(k+1)} \leftarrow \text{Update}(\mathbf{M}^{(k)})$; // cf. (33)

$k \leftarrow k + 1;$

$\mathbf{M} \leftarrow \mathbf{M}^{(k)};$

Result: \mathbf{M}

2) *Endmember estimation:* Similarly to III-B1, a direct application of the method detailed in [10], [16] yields

$$\mathbf{M}^{(k+1)} = \mathcal{P}_+ \left(\mathbf{M}^{(k)} - \frac{1}{\mu_t^{(k)}} \nabla_{\mathbf{M}} \hat{g}_t(\mathbf{M}^{(k)}) \right) \quad (33)$$

$$\mu_t^{(k)} = \gamma_2 L_{2t}, \quad \gamma_2 > 1 \quad (34)$$

where \mathcal{P}_+ is the projector on $\{\mathbf{X} | \mathbf{X} \succeq \mathbf{0}_{L,K}\}$ and L_{2t} denotes the Lipschitz constant of $\nabla_{\mathbf{M}} \hat{g}_t(\mathbf{M}_t^{(k)})$.

Note that

$$\nabla_{\mathbf{M}} \hat{g}_t(\mathbf{M}) = \mathbf{M} \left(\frac{1}{t} \mathbf{C}_t + \beta \sum_{k=1}^K \mathbf{G}_k \mathbf{G}_k^T \right) - \frac{1}{t} \mathbf{D}_t \quad (35)$$

$$L_{2t} = \left\| \frac{1}{t} \mathbf{C}_t + \beta \sum_k \mathbf{G}_k \mathbf{G}_k^T \right\|_F^2. \quad (36)$$

The resulting algorithm is summarized in Algo. 3.

C. Convergence guarantee

To ensure the convergence of the generated endmember sequence $(\mathbf{M}^{(t)})_t$ towards a critical point of the problem (18), we make the following assumptions.

Assumption 1. The quadratic functions \hat{g}_t are strictly convex and admit a Hessian matrix lower-bounded in norm by a constant $\mu_{\mathbf{M}} > 0$.

Assumption 2. The penalty functions Φ , Ψ and Υ are continuously differentiable, and gradient Lipschitz continuous with Lipschitz constant c_{Φ} , c_{Ψ} and c_{Υ} respectively.

Assumption 3. The Hessian matrix of $f(\mathbf{Y}, \mathbf{M}, \cdot, \cdot)$ – denoted by $\mathbf{H}_{(\mathbf{A}, \mathbf{dM})} f$ – is invertible at each critical point $(\mathbf{A}, \mathbf{dM})^* \in \mathcal{Q}_t(\mathbf{Y}, \mathbf{M})$ and is lower-bounded in norm by a constant $\mu > 0$.

In practice, Assumption 1 may be enforced by adding a penalization term $\frac{\mu_M}{2} \|\mathbf{M}\|_F^2$ to the objective function \hat{g}_t , where μ_M is a positive constant. Assumption 2 is only included here for the sake of completeness, in case other penalizations than those given in Section II are considered. Indeed, this assumption is obviously satisfied by the penalizations mentioned in this work. Finally, Assumption 3, which is crucial to Proposition 1, is further discussed in Appendix A to ease the reading of this paper.

Slightly adapting the arguments used in [10] to our problem, the convergence property summarized in Proposition (1) can be obtained.

Proposition 1 (Convergence of $(\mathbf{M}^{(t)})_t$, [10]). *Under the assumptions (1),(2) and (3), the distance between $\mathbf{M}^{(t)}$ and the set of critical points of the hyperspectral unmixing problem (6) converges almost surely to 0 when t tends to infinity.*

Proof: See Appendix B. ■

IV. EXPERIMENT WITH SYNTHETIC DATA

This section considers an HS image sequence composed of 10 images of size 98×102 , each image being composed of 173 bands. The images correspond to linear mixtures of 3 endmembers affected by smooth time-varying variability. The synthetic abundance maps vary smoothly from an image to another as well. Note that the pure pixel assumption is not satisfied for all the images of the times series in order to assess the algorithm performance in a challenging scenario. The synthetic linear mixtures have been corrupted by additive white Gaussian noise to ensure a resulting signal-to-noise ratio of $\text{SNR} = 30\text{dB}$. In order to introduce controlled spectral variability, the endmembers involved in the mixtures have been generated using the product of reference endmembers with randomly generated piecewise-affine functions as in [7]. The corresponding perturbed endmembers used in the experiment are depicted in Fig. 1. Note that different affine functions have been considered at each time instant for each endmember.

A. Compared methods

The results of the proposed algorithm have been compared to those obtained with two classical linear unmixing methods (VCA/SUNSAL and SISAL/SUNSAL) performed individually on each image of the time series. The methods are recalled below with their most relevant implementation details.

- 1) State-of-the-art VCA/SUNSAL (no variability): for each image, the endmembers are first extracted using the vertex component analysis (VCA) [11] which requires pure pixels to be present in the analyzed images. The abundances are then estimated for each pixel using Spectral unmixing by variable splitting and augmented Lagrangian (SUNSAL) algorithm [12];

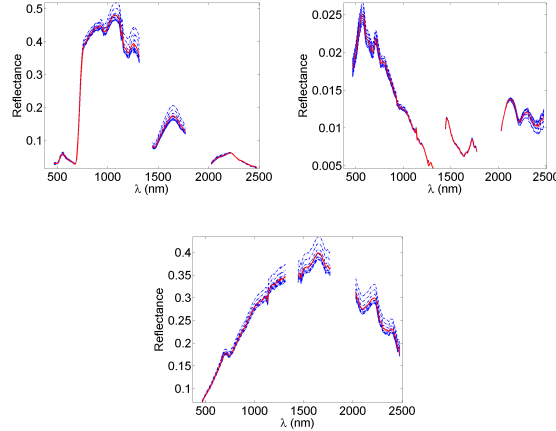


Fig. 1. Reference endmembers (red lines) and the corresponding instances under spectral variability (blue dotted lines) involved in the synthetic HS images.

- 2) SISAL/SUNSAL (no variability): the endmembers are first extracted using the simplex identification via split augmented Lagrangian [13]. Note that the pure pixel assumption is not required by this method. The tolerance for the stopping rule has been set to 10^{-2} and VCA has been used as an initialization step. The abundances are then estimated for each pixel using SUNSAL;
- 3) Proposed method: endmembers and abundances are initialized with VCA/SUNSAL, where VCA is applied to the union of the pixels belonging to the $K - 1$ convex hull of each image. The variability matrices are initialized with all their entries equal to 0. Whenever the algorithm is applied to a previously processed image, the previous abundance and variability estimates are taken as a warm-restart. The sub-problems solved by Algo. 2 and 3 are stopped after N_{iter} iterations. Finally, the global algorithm is stopped after N_{epochs} cycles – referred to as epochs – on the randomly permuted training set to approximately obtain i.i.d. samples [10]. We also included a constant forgetting factor $\xi \in (0, 1)$ in order to slowly forget the past data. The closer to one ξ is, the more slowly the past data are forgotten.

The performance of the algorithm has been assessed in terms of endmember estimation using the average spectral angle mapper (aSAM) defined as

$$\text{aSAM}(\mathbf{M}) = \frac{1}{K} \sum_{k=1}^K \frac{\langle \mathbf{m}_k | \hat{\mathbf{m}}_k \rangle}{\|\mathbf{m}_k\|_2 \|\hat{\mathbf{m}}_k\|_2} \quad (37)$$

TABLE II
PARAMETERS USED IN THE EXPERIMENTS.

	Synthetic data	Real data
σ^2	5.2	2.6
κ^2	0.52	0.13
α	7.8×10^{-3}	0
β	1.3×10^{-4}	2.13×10^{-2}
γ	3×10^{-5}	0
$\gamma_i, i \in \{1, 2, 3\}$	1.1	1.1
N_{epochs}	50	25
N_{iter}	50	50
ξ	0.99	0.99

as well as in terms of abundance and perturbation estimation through the global mean square errors (GMSEs)

$$\text{GMSE}(\mathbf{A}) = \frac{1}{TKN} \sum_{t=1}^T \|\mathbf{A}_t - \widehat{\mathbf{A}}_t\|_{\text{F}}^2 \quad (38)$$

$$\text{GMSE}(\mathbf{dM}) = \frac{1}{TLK} \sum_{t=1}^T \|\mathbf{dM}_t - \widehat{\mathbf{dM}}_t\|_{\text{F}}^2. \quad (39)$$

As a measure of fit, the following reconstruction error (RE) has been considered

$$\text{RE} = \frac{1}{TLN} \sum_{t=1}^T \|\mathbf{Y}_t - \widehat{\mathbf{Y}}_t\|_{\text{F}}^2 \quad (40)$$

$$(41)$$

where $\widehat{\mathbf{Y}}$ is the matrix formed of the pixels reconstructed with the estimated parameters.

B. Results

The parameters used for the proposed algorithm, which have been adjusted by cross-validation, are detailed in Table II. In particular, the number of cycles N_{epochs} and sub-iterations N_{iter} have been empirically chosen to obtain a compromise between the estimation accuracy and the implied computational cost. The abundance maps obtained by the proposed method are compared to those of VCA/SUNSAL in Figs. 2 to 4, whereas the corresponding endmembers are displayed in Fig. 5. The abundance maps obtained by SISAL/SUNSAL, similar to those obtained by VCA/SUNSAL, are included in a separate technical report [20], along with a more detailed version of Table III. The performance of the unmixing methods is finally reported in Table III, leading to the following conclusions.

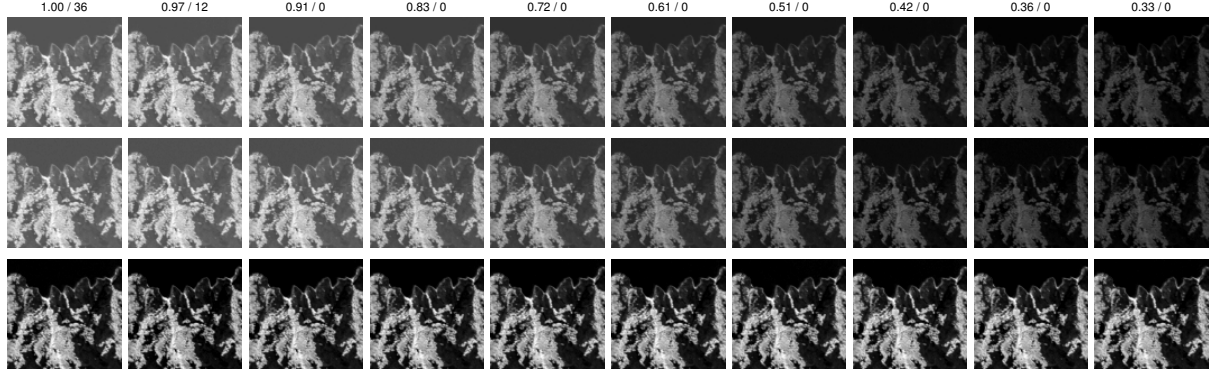


Fig. 2. Abundance maps of the first endmember used in the synthetic mixtures (theoretical abundances on the first line, proposed method on the second line, VCA/SUNSAL on the third line). The top line indicates the theoretical maximum abundance value and the true number of pixels whose abundance is greater than 0.95 for each time instant.

- The proposed method is more robust to the absence of pure pixels in some images than both VCA/SUNSAL and SISAL/SUNSAL. Indeed, the estimated abundances obtained with the proposed method (second line of Figs. 2 to 4) are closer to the ground truth (first line) than VCA/SUNSAL (third line). This observation is confirmed by the results given in Table III;
- The proposed method provides competitive unmixing results while allowing temporal endmember variability to be estimated for each endmember (see Fig. 5);
- The abundance GMSEs and the REs estimated with the proposed method are lower than those obtained with VCA/SUNSAL and SISAL/SUNSAL applied to each image individually (see Table III), without introducing much more degrees of freedom into the underlying model.

Whenever an endmember is scarcely present in one of the images, the proposed method outperforms VCA/SUNSAL as can be seen in Figs. 2 to 4. Note that the maximum theoretical abundance value and the number of pixels whose abundances are greater than 0.95 are mentioned on the top line of Figs. 2 to 4, to assess the difficulty of recovering each endmember in each image. This result was expected, since VCA is a pure pixel-based unmixing method.

V. EXPERIMENT WITH REAL DATA

A. Description of the dataset

The proposed algorithm has been applied to real HS images acquired by the Airborne Visible Infrared Imaging Spectrometer (AVIRIS) over the Lake Tahoe region (California, United States of America) between 2014 and 2015¹. Water absorption bands were removed from the 224 spectral bands,

¹The images used in this experiment are freely available from the online AVIRIS flight locator tool at http://aviris.jpl.nasa.gov/alt_locator/.

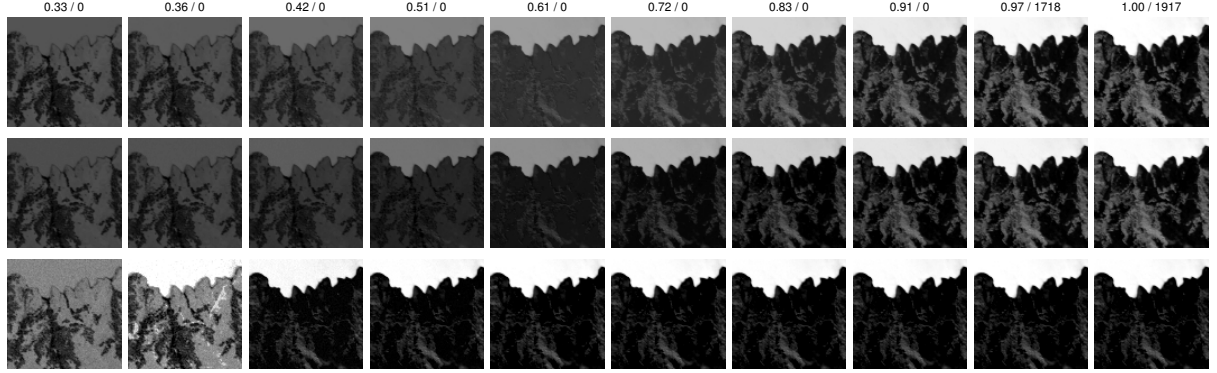


Fig. 3. Abundance maps of the second endmember used in the synthetic mixtures (theoretical abundances on the first line, proposed method on the second line, VCA/SUNSA on the third line). The top line indicates the theoretical maximum abundance value and the true number of pixels whose abundance is greater than 0.95 for each time instant.

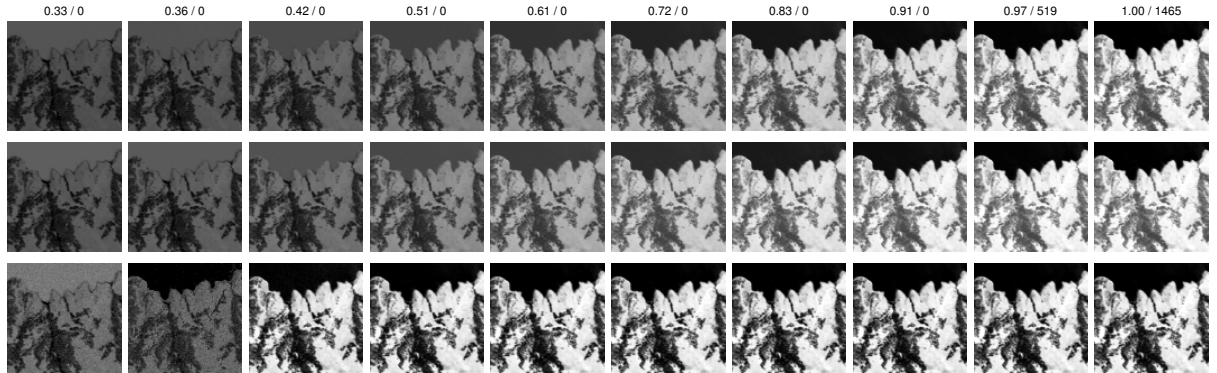


Fig. 4. Abundance maps of the third endmember used in the synthetic mixtures (theoretical abundances on the first line, proposed method on the second line, VCA/SUNSA on the third line). The top line indicates the theoretical maximum abundance value and the true number of pixels whose abundance is greater than 0.95 for each time instant.

leading to 173 exploitable spectral bands. The sub-scene of interest (150×110) is partly composed of a lake and a nearby field. Note that a 4×4 patch composed of outliers has been manually removed from the last image of the sequence prior to the unmixing procedure. The parameters used for the proposed approach are those given in Table II.

B. Results

Since no ground truth is available, the algorithm performance is evaluated in terms of the reconstruction error defined in (40). The proposed method provides lower reconstruction errors (see Table IV) and yields more consistent abundance maps, especially for the soil and the vegetation. In particular, note that the estimated vegetation abundance map of the fourth image depicted in Fig. 9 (area delineated in red) presents significant errors when visually compared to the corresponding RGB image in Fig. 6d. These errors can be explained by the fact that the water endmember extracted by

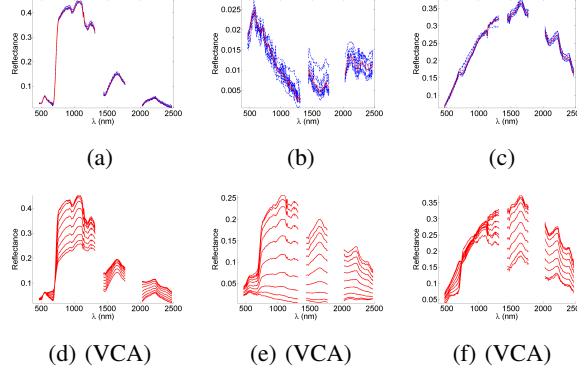


Fig. 5. Estimated endmembers on the synthetic hyperspectral time series (PLMM endmembers in red with variability in blue dotted lines on the first line, VCA-extracted endmembers on the second line, SISAL endmembers are omitted since very similar to those obtained with VCA).

TABLE III

SIMULATIONS RESULTS ON SYNTHETIC DATA (GMSE(\mathbf{A}) $\times 10^{-2}$, GMSE(\mathbf{dM}) $\times 10^{-5}$, RE $\times 10^{-5}$).

	VCA/SUNSAL	SISAL/SUNSAL	Proposed method
aSAM(\mathbf{M}) ($^{\circ}$)	15.7583	15.8830	2.1339
GMSE(\mathbf{A})	4.22	3.68	2.45×10^{-1}
GMSE(\mathbf{dM})	/	/	8.69
RE	4.13	3.75	3.77
time (s)	1	5	3120

VCA has been split into two parts as can be seen in Figs. 10d and 10f (see signatures given in black). Indeed, the VCA algorithm cannot detect the scarcely present vegetation. On the contrary, the joint exploitation of multiple images enables the faint traces of dry vegetation to be captured.

Furthermore the instantaneous variability energy (computed as $\|\mathbf{dm}_{kt}\|_2^2/L$ for $k = 1, \dots, K$ and $t = 1, \dots, T$) can reveal which endmember deviates the most from its mean spectral behavior. In this experiment, the soil and the vegetation signatures – which seem to vary the most over time (see Fig. 6) – are found by the proposed method to be affected by the most significant variability level (see Table V). In this experiment, a significant increase can be observed in the endmember variability energy over the last three images of the sequence (see Table V), suggesting that the endmembers are apparently better represented in the two first images of the sequence (see Fig. 6). This observation suggests the proposed method captures the mean endmember spectral behavior and enables the time at which the greatest spectral changes occur to be identified. However, a detailed analysis of this observation is out of the scope of the present paper.

VI. CONCLUSION AND FUTURE WORK

This paper introduced an online hyperspectral unmixing procedure accounting for endmember temporal variability based on the perturbed linear model considered in [7]. The resulting unmixing problem was formulated as a two-stage stochastic program solved by a stochastic approximation algorithm. Simulations conducted on synthetic and real data enabled the interest of the proposed approach to be appreciated. Indeed, the proposed method compared favorably with state-of-the-art approaches performed independently on each image of the sequence while providing a relevant variability estimation. Possible perspectives include the application of the proposed method to change detection problems and the extension of the method to account for spatial variability. A distributed unmixing procedure is also under investigation to solve the resulting high dimensional problem.

TABLE IV
EXPERIMENT RESULTS ON REAL DATA (RE $\times 10^{-3}$).

	VCA/FCLS	SISAL/FCLS	Proposed method
RE	1.27	1.0	1.78 $\times 10^{-1}$
time (s)	2.2	4	1214

TABLE V
EXPERIMENT WITH REAL DATA: ENERGY OF THE VARIABILITY CAPTURED FOR EACH ENDMEMBER AT EACH TIME INSTANT ($\|\mathbf{dm}_{kt}\|_2^2/L \times 10^{-5}$ FOR $k = 1, \dots, K, t = 1, \dots, T$).

	Water	Vegetation	Soil
04/10/2014	1.22	9.68	11.51
06/02/2014	1.44	11.85	38.37
09/19/2014	7.29	11.41	9.30
11/17/2014	2.77	21.73	16.55
04/29/2015	0.58	106.03	26.19

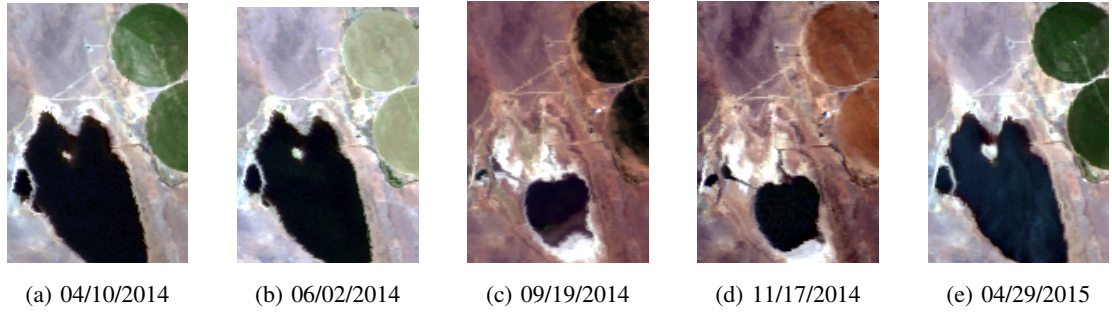


Fig. 6. Scenes used in the experiment, given with their respective acquisition date.

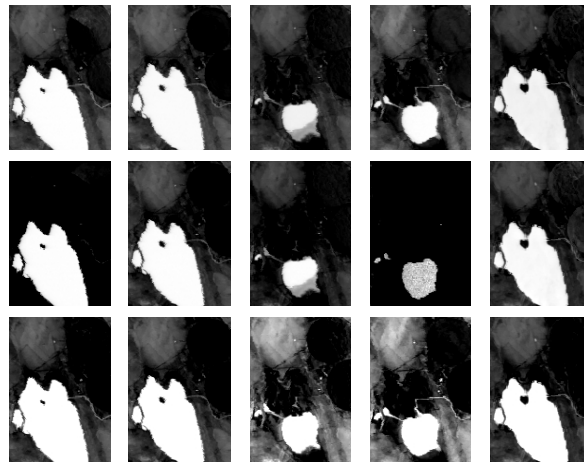


Fig. 7. Water abundance maps (proposed method on the first line, VCA/SUNSAL on the second line, SISAL/SUNSAL on the third line).

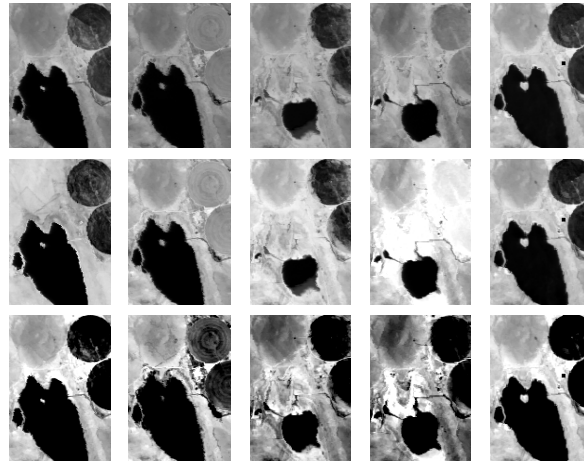


Fig. 8. Soil abundance maps (proposed method on the first line, VCA/SUNSAL on the second line, SISAL/SUNSAL on the third line).

APPENDIX A

DISCUSSION ON ASSUMPTION 3

The Hessian matrix of $f(\mathbf{Y}, \mathbf{M}, \cdot, \cdot)$, denoted by $\mathbf{H}_{(\mathbf{A}, \mathbf{dM})}f$, is given by

$$\mathbf{H}_{(\mathbf{A}, \mathbf{dM})}f = \begin{bmatrix} \mathbf{H}_1 & \mathbf{H}_2 \\ \mathbf{H}_3 & \mathbf{H}_4 \end{bmatrix} \quad \text{DRAFT (42)}$$

$$\widetilde{\mathbf{M}} = (\mathbf{M} + \mathbf{dM}) \quad (43)$$

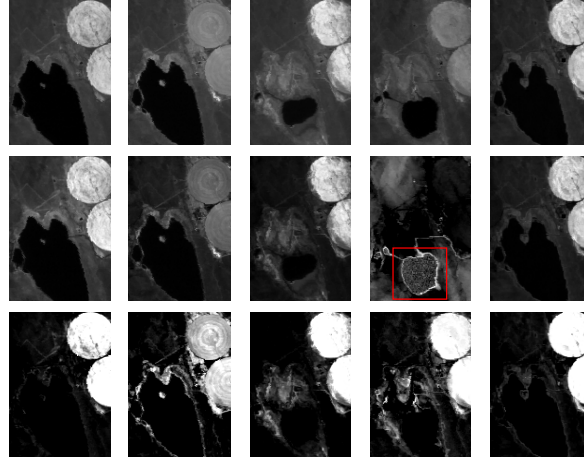


Fig. 9. Vegetation abundance maps (proposed method on the first line, VCA/SUNSAL on the second line, SISAL/SUNSAL on the third line). The region delineated in red, where almost no vegetation is supposed to be present, reveals that the water endmember extracted by VCA has been split into two parts. This observation is further confirmed in Figs. 10d and 10f.

The block matrix $\mathbf{H}_{(\mathbf{A}, \mathbf{dM})}f$ is invertible if, for instance, \mathbf{H}_1 and its Schur complement $\mathbf{H}_4 - \mathbf{H}_3\mathbf{H}_1^{-1}\mathbf{H}_2$ are invertible. In practice, \mathbf{H}_1 is generally invertible since $\mathbf{M} + \mathbf{dM}$ is full column rank. The Schur complement of \mathbf{H}_1 can be computed more explicitly, leading to

$$\begin{aligned} \mathbf{H}_4 - \mathbf{H}_3\mathbf{H}_1^{-1}\mathbf{H}_2 &= [(\mathbf{A}\mathbf{A}^T) \otimes (\mathbf{I}_L - \widetilde{\mathbf{M}}^\dagger)] \\ &\quad - [(\widetilde{\mathbf{M}}^T \widetilde{\mathbf{M}})^{-1} \otimes (\mathbf{Y} - \widetilde{\mathbf{M}}\mathbf{A})(\mathbf{Y} - \widetilde{\mathbf{M}}\mathbf{A})^T] \\ &\quad + 2\mathcal{S}(\mathbf{S}_{K,L}[(\mathbf{Y} - \widetilde{\mathbf{M}}\mathbf{A})\mathbf{A}^T \otimes \widetilde{\mathbf{M}}^\dagger]) \end{aligned} \quad (47)$$

where $\mathcal{S}(\mathbf{X})$ denotes the symmetric part of the square matrix \mathbf{X} , $\widetilde{\mathbf{M}}^\dagger$ is the pseudo-inverse of $\widetilde{\mathbf{M}}$ and $\mathbf{S}_{K,L}$ is the perfect shuffle matrix defined by

$$\mathbf{S}_{K,L} = \sum_i \sum_j \mathbf{E}_{ij}(K, L) \mathbf{E}_{ij}(K, L)^T \quad (48)$$

with $\mathbf{E}_{ij}(K, L)$ the element (i, j) of the canonical basis of $\mathbb{R}^{K \times L}$. The invertibility of (47) can be ensured via an appropriate regularization term $\frac{\mu}{2} \|\mathbf{A}, \mathbf{dM}\|_F^2$ added to the original objective f . In addition, it also enforces the lower bound assumption on the norm of $\mathbf{H}_{(\mathbf{A}, \mathbf{dM})}f$ required by Assumption 3. In fact, adding this term implies

$$\|\mathbf{H}_1\|_F \geq \mu, \quad \|\mathbf{H}_4\|_F \geq \mu \quad (49)$$

leading to

$$\|\mathbf{H}_{(\mathbf{A}, \mathbf{dM})}f\|_F^2 = \sum_{i=1}^4 \|\mathbf{H}_i\|_F^2 \geq 2\mu > 0. \quad (50)$$

APPENDIX B

CONVERGENCE PROOF

Largely adapted from [10], the following sketch of proof reduces to an adaptation of [10, Lemma 1, Proposition 1]. From this point, our problem exactly satisfies the assumptions required to apply the same arguments as in [10, Proposition 2, Proposition 3], thus recovering the announced convergence result.

Lemma 1 (Asymptotic variations of \mathbf{M}_t [10]). *Under Assumptions 1 and 2, we have*

$$\left\| \mathbf{M}^{(t+1)} - \mathbf{M}^{(t)} \right\|_F = O\left(\frac{1}{t}\right) \text{ almost surely (a.s.)}. \quad (51)$$

Proof: According to Assumption 1, \hat{g}_t is strictly convex with a Hessian lower-bounded by a scalar $\mu_M > 0$. Consequently, \hat{g}_t satisfies the second-order growth condition

$$\hat{g}_t(\mathbf{M}^{(t+1)}) - \hat{g}_t(\mathbf{M}^{(t)}) \geq \mu_M \left\| \mathbf{M}^{(t+1)} - \mathbf{M}^{(t)} \right\|_F^2. \quad (52)$$

Besides, since $\mathbf{M} \in [0, 1]^{L \times K}$, we have $\|\mathbf{M}\|_F \leq \sqrt{LK}$. Hence \hat{g}_t is Lipschitz continuous with constant $c_t = \frac{1}{t} \left(\|\mathbf{D}_t\|_F + \sqrt{LK} \|\mathbf{C}_t\|_F \right) + \beta c_\Psi$. Indeed

$$\begin{aligned} |\hat{g}_t(\mathbf{M}_1) - \hat{g}_t(\mathbf{M}_2)| &\leq \beta |\Psi(\mathbf{M}_1) - \Psi(\mathbf{M}_2)| + \\ &\frac{1}{t} \left| \frac{1}{2} \langle \mathbf{M}_1^T \mathbf{M}_1 - \mathbf{M}_2^T \mathbf{M}_2, \mathbf{C}_t \rangle - \langle \mathbf{M}_1 - \mathbf{M}_2, \mathbf{D}_t \rangle \right| \\ &\leq \frac{1}{t} \left(\frac{1}{2} \left\| \mathbf{M}_1^T \mathbf{M}_1 - \mathbf{M}_2^T \mathbf{M}_2 \right\|_F \|\mathbf{C}_t\|_F + \|\mathbf{M}_1 - \mathbf{M}_2\|_F \|\mathbf{D}_t\|_F \right) \\ &\quad + \beta c_\Psi \|\mathbf{M}_1 - \mathbf{M}_2\|_F \end{aligned} \quad (53)$$

where \mathbf{C}_t and \mathbf{D}_t were defined in (11). In addition

$$\begin{aligned} \left\| \mathbf{M}_1^T \mathbf{M}_1 - \mathbf{M}_2^T \mathbf{M}_2 \right\|_F &= \\ \left\| \frac{1}{2} (\mathbf{M}_1 + \mathbf{M}_2)^T (\mathbf{M}_1 - \mathbf{M}_2) + \frac{1}{2} (\mathbf{M}_1 - \mathbf{M}_2)^T (\mathbf{M}_1 + \mathbf{M}_2) \right\|_F \\ &\leq \|\mathbf{M}_1 + \mathbf{M}_2\|_F \|\mathbf{M}_1 - \mathbf{M}_2\|_F \leq 2\sqrt{LK} \|\mathbf{M}_1 - \mathbf{M}_2\|_F \end{aligned} \quad (54)$$

hence

$$|\hat{g}_t(\mathbf{M}_1) - \hat{g}_t(\mathbf{M}_2)| \leq c_t \|\mathbf{M}_1 - \mathbf{M}_2\|_F. \quad (55)$$

Combining (52) and (55), we have

$$\left\| \mathbf{M}^{(t+1)} - \mathbf{M}^{(t)} \right\|_F \leq \frac{c_t}{\mu_M}. \quad (56)$$

Since the data, the abundances and the variability are respectively contained in compact sets, \mathbf{C}_t and \mathbf{D}_t are (almost surely) bounded, thus: $c_t = O\left(\frac{1}{t}\right)$ a.s. ■

Proposition 2 (Adapted from [10]). *We assume that the requirements in Assumption 1 to 3 are satisfied. For $(\mathbf{Y}, \mathbf{M}) \in \mathcal{Y} \times \mathcal{M}$, let us define*

$$(\mathbf{A}^*, \mathbf{dM}^*) \in \arg \min_{(\mathbf{A}, \mathbf{dM}) \in \mathcal{A}_K \times \mathcal{D}} f(\mathbf{Y}, \mathbf{M}, \mathbf{A}, \mathbf{dM}) \quad (57)$$

$$z(\mathbf{Y}, \mathbf{M}) = f(\mathbf{Y}, \mathbf{M}, \mathbf{A}^*, \mathbf{dM}^*). \quad (58)$$

Then

1) the function z is continuously differentiable with respect to \mathbf{M} and

$$\nabla_{\mathbf{M}} z(\mathbf{Y}, \mathbf{M}) = \nabla_{\mathbf{M}} f(\mathbf{Y}, \mathbf{M}, \mathbf{A}^*, \mathbf{dM}^*); \quad (59)$$

2) g defined in (6) is continuously differentiable and $\nabla_{\mathbf{M}} g(\mathbf{M}) = \mathbb{E}_{\mathbf{Y}} [\nabla_{\mathbf{M}} z(\mathbf{Y}, \mathbf{M})]$;
3) $\nabla_{\mathbf{M}} g(\mathbf{M})$ is Lipschitz continuous on \mathcal{M} .

Proof: The existence of $(\mathbf{A}^*, \mathbf{dM}^*)$ follows from the continuity of $f(\mathbf{Y}, \mathbf{M}, \cdot, \cdot)$, which is minimized on a compact subset of $\mathbb{R}^{K \times N} \times \mathbb{R}^{L \times K}$. Assumption 3 ensures that the critical points of $f(\mathbf{Y}, \mathbf{M}, \cdot, \cdot)$ are locally unique, and thus that $(\mathbf{A}^*, \mathbf{dM}^*)$ is locally unique. Indeed, in practice, for a given (\mathbf{Y}, \mathbf{M}) and an initial $(\mathbf{A}_0, \mathbf{dM}_0)$, there exists a neighborhood V of $(\mathbf{A}_0, \mathbf{dM}_0)$ such that $f(\mathbf{Y}, \mathbf{M}, \cdot, \cdot)$ admits a unique critical point on $(\mathcal{A}_K \times \mathcal{D}) \cap V$, denoted by $(\mathbf{A}^*, \mathbf{dM}^*)$, to which the PALM algorithm converges.

Since $(\mathbf{A}^*, \mathbf{dM}^*)$ is (locally) unique, the theorem recalled in [10, Theorem 1] can be directly applied to get the first statement. The second statement follows from the continuous differentiability of $z(\mathbf{Y}, \cdot)$, defined on a compact set.

To prove the third point, it is sufficient to show that $(\mathbf{A}^*, \mathbf{dM}^*)$, considered as a function of \mathbf{M} , is Lipschitz continuous with a constant independent of \mathbf{Y} . This point follows from Assumption 3 and arguments similar to those given in [9, Step 1 p. 587], which concludes the proof. ■

REFERENCES

- [1] J. M. Bioucas-Dias, A. Plaza, N. Dobigeon, M. Parente, Q. Du, P. Gader, and J. Chanussot, “Hyperspectral unmixing overview: Geometrical, statistical, and sparse regression-based approaches,” *IEEE J. Sel. Topics Appl. Earth Observ. in Remote Sens.*, vol. 5, no. 2, pp. 354–379, April 2012.
- [2] A. Zare and K. C. Ho, “Endmember variability in hyperspectral imagery,” *IEEE Signal Process. Mag.*, vol. 31, no. 1, pp. 95–104, Jan. 2014.
- [3] O. Eches, N. Dobigeon, C. Mailhes, and J.-Y. Tourneret, “Bayesian estimation of linear mixtures using the normal compositional model. Application to hyperspectral imagery,” *IEEE Trans. Image Process.*, vol. 19, no. 6, pp. 1403–1413, June 2010.
- [4] X. Du, A. Zare, P. Gader, and D. Dranishnikov, “Spatial and spectral unmixing using the beta compositional model,” *IEEE J. Sel. Topics Appl. Earth Observ. in Remote Sens.*, vol. 7, no. 6, pp. 1994–2003, June 2014.
- [5] A. Halimi, N. Dobigeon, and J.-Y. Tourneret, “Unsupervised unmixing of hyperspectral images accounting for endmember variability,” *IEEE Trans. Image Process.*, vol. 24, no. 12, pp. 4904–4917, Dec. 2015.

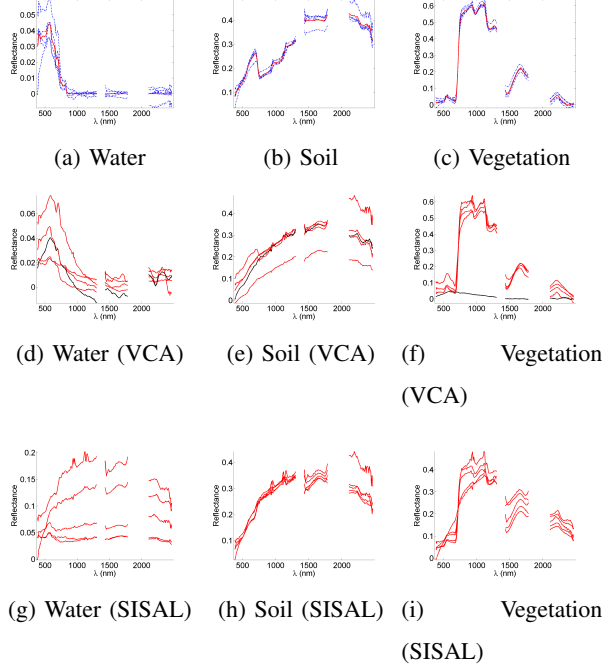


Fig. 10. Endmembers and variability (endmembers in red lines, variability in blue dashed lines) recovered by the proposed method on the first line, VCA-extracted endmembers on the second line, SISAL-extracted endmembers on the third line. The endmembers given in black on the second line correspond to the endmembers identified by VCA on the image 6d, where the water endmember has been split into two parts (see Figs. 10d and 10f).

- [6] B. Somers, M. Zortea, A. Plaza, and G. Asner, “Automated extraction of image-based endmember bundles for improved spectral unmixing,” *IEEE J. Sel. Topics Appl. Earth Observ. in Remote Sens.*, vol. 5, no. 2, pp. 396–408, April 2012.
- [7] P.-A. Thouvenin, N. Dobigeon, and J.-Y. Tourneret, “Hyperspectral unmixing with spectral variability using a perturbed linear mixing model,” *IEEE Trans. Signal Process.*, 2015, to appear. [Online]. Available: <http://arxiv.org/abs/1502.01260>
- [8] A. Halimi, N. Dobigeon, J.-Y. Tourneret, S. McLaughlin, and P. Honeine, “Unmixing hyperspectral images accounting for temporal and spatial endmember variability,” in *Proc. European Signal Process. Conf. (EUSIPCO)*, Nice, France, Aug. 2015, to appear.
- [9] D. Ralph and H. Xu, “Convergence of stationary points of sample average two-stage stochastic programs: A generalized equation approach,” *Mathematics of Operations Research*, vol. 36, no. 3, pp. 568–592, Aug. 2011.
- [10] J. Mairal, F. Bach, J. Ponce, and G. Sapiro, “Online learning for matrix factorization and sparse coding,” *J. Mach. Learning Research*, vol. 11, pp. 19–60, Jan. 2010.
- [11] J. M. Nascimento and J. M. Bioucas-Dias, “Vertex component analysis: a fast algorithm to unmix hyperspectral data,” *IEEE Trans. Geosci. Remote Sens.*, vol. 43, no. 4, pp. 898–910, April 2005.
- [12] J. M. Bioucas-Dias and M. A. T. Figueiredo, “Alternating direction algorithms for constrained sparse regression: Application to hyperspectral unmixing,” in *Proc. IEEE GRSS Workshop Hyperspectral Image Signal Process.: Evolution in Remote Sens. (WHISPERS)*, Reykjavik, Iceland, June 2010.
- [13] J. M. Bioucas-Dias, “A variable splitting augmented Lagrangian approach to linear spectral unmixing,” in *Proc. IEEE GRSS Workshop Hyperspectral Image Signal Process.: Evolution in Remote Sens. (WHISPERS)*, Grenoble, France, Aug. 2009.
- [14] M. Berman, H. Kiiveri, R. Lagerstrom, A. Ernst, R. Dunne, and J. F. Huntington, “ICE: A statistical approach to

identifying endmembers in hyperspectral images," *IEEE Trans. Geosci. Remote Sens.*, vol. 42, no. 10, pp. 2085–2095, Oct. 2004.

[15] M. Arngren, M. N. Schmidt, and J. Larsen, "Unmixing of hyperspectral images using Bayesian nonnegative matrix factorization with volume prior," *J. Signal Process. Sys.*, vol. 65, no. 3, pp. 479–496, Nov. 2011.

[16] J. Bolte, S. Sabach, and M. Teboulle, "Proximal alternating linearized minimization for nonconvex and nonsmooth problems," *Mathematical Programming*, vol. 1-2, no. 146, pp. 459–494, July 2013.

[17] J. Duchi, S. Shalev-Schwartz, Y. Singer, and T. Chandra, "Efficient projection onto the ℓ_1 -ball for learning in high dimensions," in *Proc. Int. Conf. Machine Learning (ICML)*, Helsinki, Finland, 2008.

[18] L. Condat, "Fast projection onto the simplex and the ℓ_1 ball," *Math. Program., Ser. A*, 2015, to appear.

[19] S. Becker, E. J. Candès, and M. Grant, "Templates for convex cone problems with applications to sparse signal recovery," *Math. Prog. Comp.*, vol. 3, no. 3, pp. 165–218, Sept. 2011.

[20] P.-A. Thouvenin, N. Dobigeon, and J.-Y. Tourneret, "Online unmixing of multitemporal hyperspectral images accounting for spectral variability – complementary results," University of Toulouse, IRIT/INP-ENSEEIHT, France, Tech. Rep., Oct. 2015. [Online]. Available: http://thouvenin.perso.enseeiht.fr/papers/Thouvenin_TR_2015.pdf

Pierre-Antoine Thouvenin (S'15) received the state engineering degree in electrical engineering from ENSEEIHT, Toulouse, France, and the M.Sc. degree in signal processing from the National Polytechnic Institute of Toulouse (INP Toulouse), both in 2014. He is currently working toward the Ph.D. degree within the Signal and Communications Group of the IRIT Laboratory, Toulouse, France. His research is currently focused on hyperspectral unmixing and variability modeling in hyperspectral imagery.

Nicolas Dobigeon (S'05–SM'08–SM'13) received the state engineering degree in electrical engineering from ENSEEIHT, Toulouse, France, and the M.Sc. degree in signal processing from the National Polytechnic Institute of Toulouse (INP Toulouse), both in June 2004, as well as the Ph.D. degree and Habilitation à Diriger des Recherches in Signal Processing from the INP Toulouse in 2007 and 2012, respectively. He was a Post-Doctoral Research Associate with the Department of Electrical Engineering and Computer Science, University of Michigan, Ann Arbor, MI, USA, from 2007 to 2008.

Since 2008, he has been with the National Polytechnic Institute of Toulouse (INP-ENSEEIHT, University of Toulouse) where he is currently an Associate Professor. He conducts his research within the Signal and Communications Group of the IRIT Laboratory and he is also an affiliated faculty member of the Telecommunications for Space and Aeronautics (TeSA) cooperative laboratory. His current research interests include statistical signal and image processing, with a particular interest in Bayesian inverse problems with applications to remote sensing, biomedical imaging and genomics.

Jean-Yves Tourneret (SM'08) received the ingénieur degree in electrical engineering from the Ecole Nationale Supérieure d'Electronique, d'Electrotechnique, d'Informatique, d'Hydraulique et des Télécommunications (ENSEEIHT) de Toulouse in 1989 and the Ph.D. degree from the National Polytechnic Institute from Toulouse in 1992. He is currently a professor in the university of Toulouse (ENSEEIHT) and a member of the IRIT laboratory (UMR 5505 of the CNRS). His research activities are centered around statistical signal and image processing with a particular interest to Bayesian and Markov chain Monte Carlo (MCMC) methods. He has been involved in the organization of several conferences including the European conference on signal processing EUSIPCO'02 (program chair), the international conference ICASSP'06 (plenaries), the statistical signal processing workshop SSP'12 (international liaisons), the International Workshop on Computational Advances in Multi-Sensor Adaptive Processing CAMSAP 2013 (local arrangements), the statistical signal processing workshop SSP'2014 (special sessions), the workshop on machine learning for signal processing MLSP'2014 (special sessions). He has been the general chair of the CIMI workshop on optimization and statistics in image processing hold in Toulouse in 2013 (with F. Malgouyres and D. Kouamé) and of the International Workshop on Computational Advances in Multi-Sensor Adaptive Processing CAMSAP 2015 (with P. Djuric). He has been a member of different technical committees including the Signal Processing Theory and Methods (SPTM) committee of the IEEE Signal Processing Society (2001-2007, 2010-present). He has been serving as an associate editor for the IEEE Transactions on Signal Processing (2008-2011, 2015-present) and for the EURASIP journal on Signal Processing (2013-present).